metals

MDPI

Article

Effect of Small Variations in Zr Content on the Microstructure and Properties of Ferritic ODS Steels Consolidated by SPS

Andrea García-Junceda [1,*], Eric Macía [2], Dariusz Garbiec [3], Marta Serrano [4], José M. Torralba [1,2] and Mónica Campos [2]

1 IMDEA Materials Institute, C/ Eric Kandel 2, 28906 Getafe, Madrid, Spain; josemanuel.torralba@imdea.org
2 Dept. Materials Science and Engineering, IABB, Universidad Carlos III de Madrid (UC3M), Av. de la Universidad 30, 28911 Leganés, Madrid, Spain; emacia@ing.uc3m.es (E.M.); campos@ing.uc3m.es (M.C.)
3 Łukasiewicz Research Network - Metal Forming Institute, Jana Pawla II 14, 61-139 Poznan, Poland; dariusz.garbiec@inop.poznan.pl
4 Structural Materials Division, CIEMAT, Av. de la Complutense 22, 28040 Madrid, Spain; marta.serrano@ciemat.es
* Correspondence: andrea.garcia.junceda@imdea.org; Tel.: +34-915493522

Received: 18 February 2020; Accepted: 4 March 2020; Published: 6 March 2020

Abstract: Two different zirconium contents (0.45 and 0.60 wt.%) have been incorporated into a Fe-14Cr-5Al-3W-0.4Ti-0.25Y_2O_3 oxide dispersion-strengthened (ODS) steel in order to evaluate their effect on the final microstructure and mechanical properties. The powders with the targeted compositions were obtained by mechanical alloying (MA), and subsequently processed by spark plasma sintering (SPS) at two different heating rates: 100 and 400 °C·min^{-1}. Non-textured bimodal microstructures composed of micrometric and ultrafine grains were obtained. The increase in Zr content led to a higher percentage of Zr nano-oxides and larger regions of ultrafine grains. These ultrafine grains also seem to be promoted by higher heating rates. The effective pinning of the dislocations by the Zr dispersoids, and the refining of the microstructure, have significantly increased the strength exhibited by the ODS steels during the small punch tests, even at high temperatures (500 °C).

Keywords: ODS; zirconium; spark plasma sintering (SPS); microstructure; small punch test (SP)

1. Introduction

The harsh environments that will stand the Generation IV nuclear fission reactors have motivated the need of using materials capable to resist these extreme conditions. Within this framework, FeCrAl oxide dispersion-strengthened (ODS) steels have been considered in the past decades to withstand both the high operation temperatures and the neutron fluxes [1,2]. The properties of ODS steels result from the combination of high density of thermally stable nano-oxides homogenously distributed in the matrix, which are able to pin dislocations increasing the creep behaviour, and the fine grain size distribution that promotes high strength [3,4].

Initially, the oxides particles were pure Y_2O_3, which seem to be fragmented during the milling step and then become partially amorphous [5]. However, this addition of Y_2O_3 was not enough to improve the mechanical properties. Thus, Ti was added to promote finer nano-oxides more resistant to the coarsening [6]. Furthermore, W was also incorporated in order to increase the properties at high temperature by solid solution strengthening and to decrease the creep strain rate [7]. In those cases where special requirements of corrosion resistance were needed, such as materials dealing with liquid metals and supercritical water, Al and Cr were suitable elemental candidates in order to improve the

resistance [8,9]. Nevertheless, the addition of Al has been reported by many authors as responsible for the coarsening of the oxides because of the formation of Y-Al-O particles [8,10,11]. This oxide growth decreases the strength at high temperature. Therefore, the option of adding a new element such as Zr has been investigated in recent years to avoid the coarsening of the oxides while keeping the mechanical strength and the corrosion resistance [12,13]. The reason for these improvements is that the binding energy of Y-Zr oxides in an iron matrix is higher than that of Y-Al oxides, indicating that Y-Zr oxides are formed more easily and with higher stability than Y-Al oxide particles, refining the oxide particles and increasing their number density [12,14]. Furthermore, the incorporation of Zr introduces the additional benefit of increasing the resistance to irradiation damage due to the high irradiation tolerance and thermal stability introduced by these new nano-oxides [12,15].

On the other hand, the most common processing routes used to sinter ODS steels are hot extrusion (HE) and hot isostatic pressing (HIP). However, in the last years, field assisted sintering techniques (FAST), such as spark plasma sintering (SPS) and field-assisted hot pressing (FAHP), have been reported as promising processes to better tailor a suitable bimodal grain structure [16–18]. This grain size distribution is mainly composed of micrometric and nanometric grains. On one side, the micrometric grains have a direct effect on the increase of the ductility, since they improve the strain hardening mechanism by promoting the dislocation activity. On the other side, the fine nanometric grains improve the strength as a result of a higher quantity of grain boundaries acting as a barrier for the dislocation movement [19]. Therefore, it is possible to obtain a hetero-nanostructure in which the material possesses high strength together with an adequate ductility. One important advantage of this FAST techniques, in which powders are poured into a graphite matrix and undergo simultaneous uniaxial pressing and heating by the Joule effect, is that they allow the consolidation of the samples in short periods of time (around 30–40 min or even lower times) [20,21]. This fact is due to the fast generation of internal heat that increases the sintering kinetics and leads to higher densifications. Therefore, an undesirable growth of the nano-oxides and the austenitic grains, transforming into ferrite during the cooling of the ODS steels analysed in this work, is partially avoided during the sintering step.

In the present investigation, a FeCrAlW-ODS pre-alloyed powder is modified by adding elemental Ti, Y_2O_3 and Zr or ZrO_2 during the mechanical alloying with. The aim is to analyse the effect of the Zr nano-oxides on the final properties achieved after SPS. This Zr is incorporated with two different weight percentages, 0.45 and 0.60 wt.%. Thus, the final concentration in each sample will be different in order to discern if small differences in the final Zr content of the sample may affect the final mechanical properties at room and high temperatures. All materials are mechanically evaluated by Vickers hardness (HV) and small punch testing (SPT) at different temperatures. These results are also compared to those reported for the 14Cr ODS material characterised in the framework of the GETMAT European project (14GET) in order to further qualify the new steels [22].

2. Materials and Methods

The ODS steels developed in this investigation were obtained by MA of a prealloyed Fe-14Cr-5Al-3W (wt.%) powder supplied by Sandvik Osprey (Neath Port Talbot, UK), a high pure elemental Ti powder provided by GfE mbH (Nuremberg, Germany), an Y_2O_3 nanopowder from TJ Technologies & Materials Inc. (Shanghai, China), and two different powders acting as Zr sources: a ZrO_2 powder provided by Arenas Minerales S.L. (Castellón, Spain) and a pure elemental Zr powder from Good Fellow (Hamburg, Germany). Two different contents of Zr were selected: 0.45 and 0.60 wt.%. The nominal compositions for the ODS powders are listed in Table 1.

For the chemical analysis of the oxygen content in the powders, a LECO TC500 analyser (St. Joseph, MI, USA) was used, whereas a LECO CS230 analyser (St. Joseph, MI, USA) was utilised for the measurement of the carbon content. The morphology and shape of the powders were assessed by means of a Zeiss EVO MA15 scanning electron microscope (Oberkochen, Germany) at an accelerating voltage of 20 kV. Furthermore, the particle size distribution was evaluated by a laser particle size

analyser (Mastersizer 2000, Malvern, Worcestershire, UK). In order to characterise the crystallite size and lattice strain after the milling of the powders, X-ray diffraction was performed using the Cu K_α radiation of a Philips X'pert diffractometer (Amsterdam, The Netherlands) and the calculations were made applying the Scherrer method [23].

Table 1. Nominal composition and Zr content of ODS powders (wt.%).

Sample ID	Composition	Zr Content
ODS_NoZr	Fe-14Cr-5Al-3W-0.4Ti-0.25Y_2O_3	Null
ODS_0.45Zr	Fe-14Cr-5Al-3W-0.4Ti-0.25Y_2O_3-0.6ZrO_2	0.45
ODS_0.60Zr	Fe-14Cr-5Al-3W-0.4Ti-0.25Y_2O_3-0.6Zr	0.60

The ODS steels were consolidated by SPS using HP D 25/3 furnace (FCT Systeme GmbH, Frankenblick, Germany) under low vacuum (5×10^{-2} mbar). The powders were poured into a graphite die of 20 mm diameter and sintered at 1100 °C. Two different heating rates were selected, 100 and 400 °C·min^{-1}, to analyse their effect on the final properties. The dwelling time was 5 min with a compacting pressure of 80 MPa. A high purity tungsten foil (25 μm thick) was used in order to avoid a potential carbon contamination coming from the graphite tools [24,25].

The microstructure was characterised using a dual-beam scanning electron microscope FEG-FIB Helios Nanolab 600i (FEI, Hilsboro, OR, USA) coupled to electron backscatter diffraction (EBSD-Oxford Instruments HKL NordlysNano detector, Oxford, UK). The sintered samples were ground with SiC papers and subsequently polished down to 1 μm with diamond solutions. A colloidal silica solution was used at the final stage to slightly etch the samples and to remove the deformation layer produced during mechanical polishing. The EBSD acquisitions were conducted with an accelerating voltage of 15 kV, a beam current of 5.5 nA and a step size equal to 80 nm. The average austenite grain sizes were calculated using the post-processing software HKL Channel 5.0 supplied by Oxford Instruments (Oxford, UK), considering grain boundaries with misorientation angles above 5°. With the aim of characterising the composition of the different oxides present within the ferritic matrix of the SPSed samples, Z-contrast imaging by high angle annular dark field scanning transmission electron microscopy (HAADF) and EDX elemental mapping analyses were performed in FIB samples using a Talos F200X FEI TEM (Hilsboro, OR, USA) operating at 200 kV. TEM lamellas extraction was carried out using the dual-beam scanning electron microscope described above, which was equipped with a gallium liquid metal ion source. The system has an Omniprobe TM micromanipulator to control a tungsten needle and a Pt-gas injection system to cover and protect the site of interest with a stripe of platinum. The surrounding material is then etched away using the Ga-ion beam. With this aim, an acceleration voltage of 30 kV is applied and the ion beam current is progressively decreased from 65 nA to 0.79 nA. In this step, the final thickness achieved is around 1.5 μm. The tungsten needle is subsequently used to extract and move the lamella to a V-shaped copper holder, where it is fixed by Pt deposition. At this moment, the Ga-ion beam current is decreased to 16 pA with a voltage of 5 kV to minimize the beam damage and to polish the lamella progressively on both sides to a final homogeneous thickness of 100 nm.

The evaluation of the mechanical properties was carried out by means of Vickers microhardness measurements and small punch tests. For microhardness tests, a load of 0.2 kg during 10 s was applied in a SHIMADZU HMV-2 tester (Kyoto, Japan) equipped with a Vickers diamond indenter. The hardness data correspond to the average of ten measurements. To assess the fracture behaviour of the ODS steels with temperature by SPT, 3-mm diameter discs were cut in the transverse section to the sintering pressure. Plane-parallel samples with a thickness of 0.250 mm were obtained by grinding and polishing both sides of the disc using colloidal silica at the final stage. The tests were performed at three different temperatures (R.T., 300 and 500 °C) with a puncher tip diameter of 1 mm and at a rate displacement of 0.3 mm·min^{-1}, following The European Code of Practice for Small Punch Testing

for Tensile and Fracture Behaviour [26]. The test was repeated twice in each condition to ensure its reproducibility.

3. Results and Discussion

3.1. Characterisation of MA ODS Powders

An adequate milling of ODS powders is an important step to assure the limitation of the ferritic grain size and nano-oxides growth during the sintering by SPS. High-energy ball milling basically consists of repeated fragmentation, cold welding, dynamic recrystallisation and mechanically driven interdiffusion in order to convert the raw powders into a single phase alloy. The irregular shape of the MA ODS powders with 0.45 or 0.60 wt.% of Zr is shown in Figure 1.

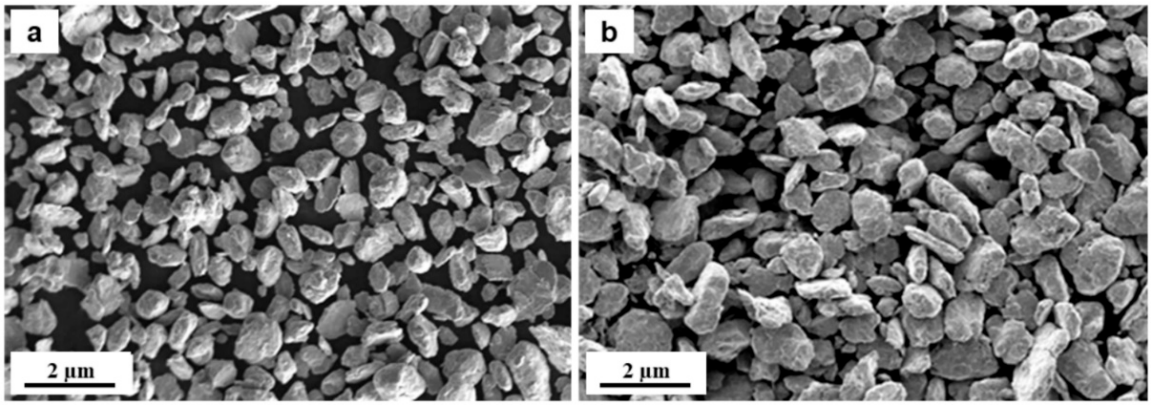

Figure 1. Powder morphology after 50 h of milling: (**a**) ODS-0.45Zr, (**b**) ODS-0.60Zr.

The powders of this investigation were characterised in terms of mean particle size, oxygen/carbon contents and crystallographic parameters, as listed in Table 2. The MA process provides a high density of dislocations, which decreases significantly the crystalline coherence zone and leads to the reduction of the crystal size of the ODS powders in comparison with the prealloyed powders. On the other hand, it is worth highlighting the increase of the lattice strain as a result of the distortions introduced in the system due to the incorporation of Ti, Y, Zr and O into the lattice [27]. The crystallite size and the microstrain values achieved after 50 h of milling time at 800 rpm are suitable parameters for retaining the nanostructure during the sintering, since the crystal growth begins when the internal strain decreases below a certain value dependent on the material [28,29].

Table 2. Mean particle size, interstitial contents and crystallographic parameters of the powders.

Sample ID	d_{50} (µm)	O (wt.%)	C (wt.%)	Crystallite Size (nm)	Lattice Strain (%)
Prealloyed 14Cr	29.8	0.030	0.012	43.1	0.217
ODS_NoZr	49.9	0.350	0.141	13.8	0.760
ODS_0.45Zr	44.8	0.188	0.048	12.4	0.836
ODS_0.60Zr	77.0	0.047	0.195	11.7	0.782

3.2. Microstructural Characterisation of SPS ODS Alloys

The microstructure of the ODS steels sintered by SPS with different heating rates (100 and 400 °C·min^{-1}) was analysed by using the Inverse Pole Figure (IPF) maps obtained after the acquisition by EBSD (Figure 2).

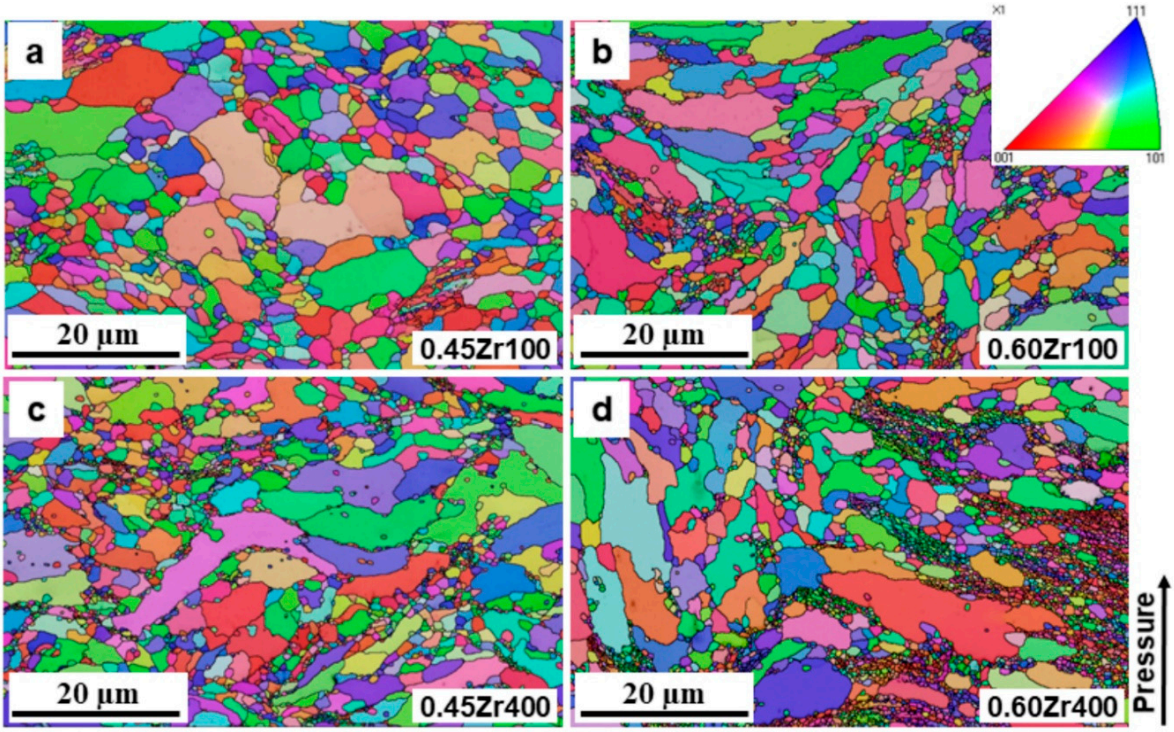

Figure 2. IPF-EBSD maps on the ODS alloys: (**a**) ODS-0.45Zr100 sintered at 100 °C·min^{-1}, (**b**) ODS-0.6Zr100 sintered at 100 °C·min^{-1}, (**c**) ODS-0.45Zr400 sintered at 400 °C·min^{-1}, (**d**) ODS-0.60Zr400 sintered at 400 °C·min^{-1}.

As shown in this figure, a SPS process usually generates a bimodal grain-size nanostructure because of different phenomena acting together: generation of non-homogeneous spatial distribution of stored energies during MA, non-uniform distribution of oxides and heterogeneous temperature distribution within the powders during sintering [30]. From these maps, it can be noted that the introduction of a higher zirconium content into the system has led to the increase of the ultrafine-grained areas (grain size below 1 µm) within the matrix for the same sintering condition. The refinement of the microstructure may be probably due to the precipitation of a higher quantity of effective Zr nano-oxides acting as inhibitors of the grain size growth during recrystallisation. On the other hand, the increase of the heating rate during the SPS also has a clear effect on the final microstructure reached, leading to more regions of ultrafine grains for the same ODS composition, as previously reported by Macía et al. [17] This may be caused by a higher heating rate leading to shorter times to homogeneously distribute the heat generated by the Joule effect through the powders, in physical contact inside the sintering die, producing as a result bigger grains in those regions in which the temperature reaches higher values.

The size and composition of the oxides generated in the ODS steels are evaluated, since they have a close effect on the final grain size achieved, and subsequently on the mechanical properties at room and high temperatures. For the whole study of the oxides, the samples heated at 100 °C·min^{-1} were selected. The addition of Zr during the MA is mainly seeking for the refinement of the oxides and it would contribute to the increase of the oxide density. As shown in Figure 3, the oxide dispersoids are not homogeneously distributed within the different grains. Therefore, it is possible to find grains with higher oxide number density. Most of the particles are in a range size between 3 and 25 nm, and they are located inside the grains and along the grain boundaries.

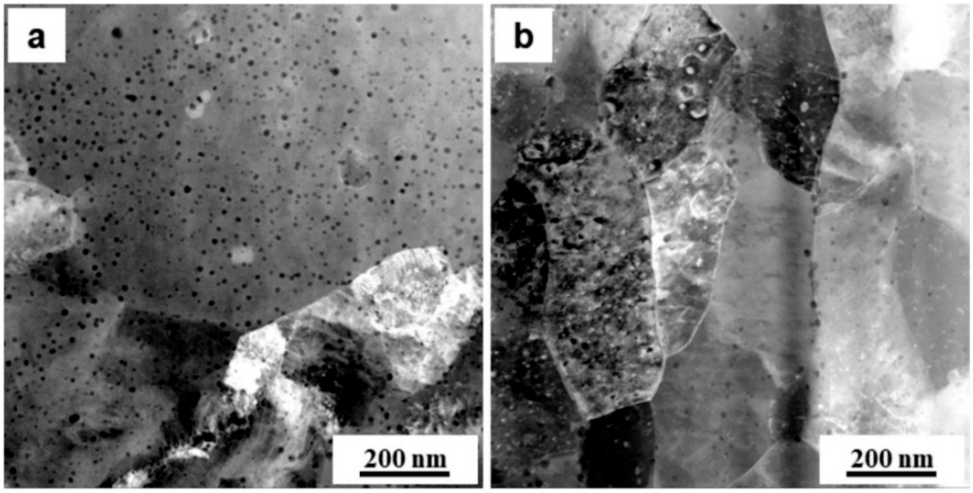

Figure 3. Bright field STEM images: (**a**) ODS-0.45Zr, (**b**) ODS-0.60Zr.

The oxide size distribution and the mean oxide diameter are calculated from representative dark field TEM micrographs (Figure 4). These histograms indicate that the mean oxide diameter is 7.7 nm for ODS-0.45Zr and 5.6 nm for ODS-0.60Zr, whereas it is 12.0 nm in the sample without Zr. Therefore, the oxide size has been refined by adding Zr, which is able to form fine and more stable nano-oxides, as reported by several authors [12,31]. The oxide number densities reached in the ultrafine regions are in the same order of magnitude for both ODS samples with Zr, being 1.4×10^{22} m^{-3} in the case of the ODS with the lower Zr content and 1.6×10^{22} m^{-3} for the ODS with 0.6 wt.% of Zr. The previous values represent an increase in an order of magnitude with respect to the ODS without Zr, which oxide number density is 5.6×10^{21} m^{-3}.

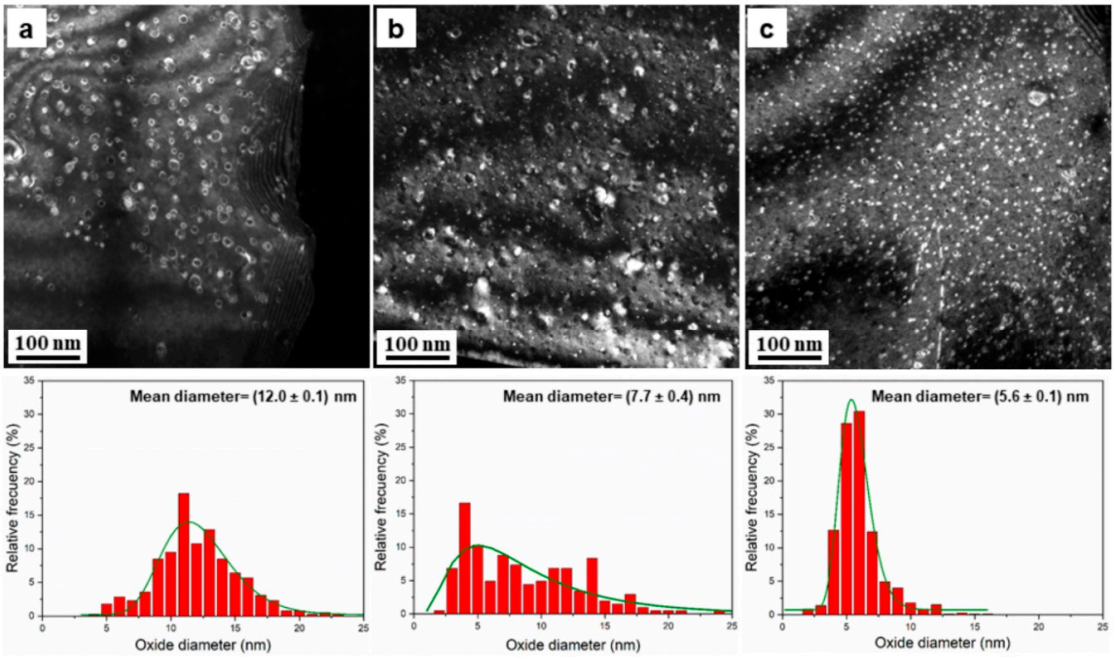

Figure 4. TEM images and oxide size distribution: (**a**) ODS-NoZr, (**b**) ODS-0.45Zr, (**c**) ODS-0.60Zr.

To characterise the elements that are forming the nano-oxides, TEM EDX maps were obtained in different regions, similar to those shown in Figure 5, in both ODS with different Zr contents. Around two hundred oxides were analysed for each ODS sample and it is worth mentioning that almost all 1-, 2-, 3- or 4-element combinations among Y, Al, Ti, and Zr with oxygen are possible.

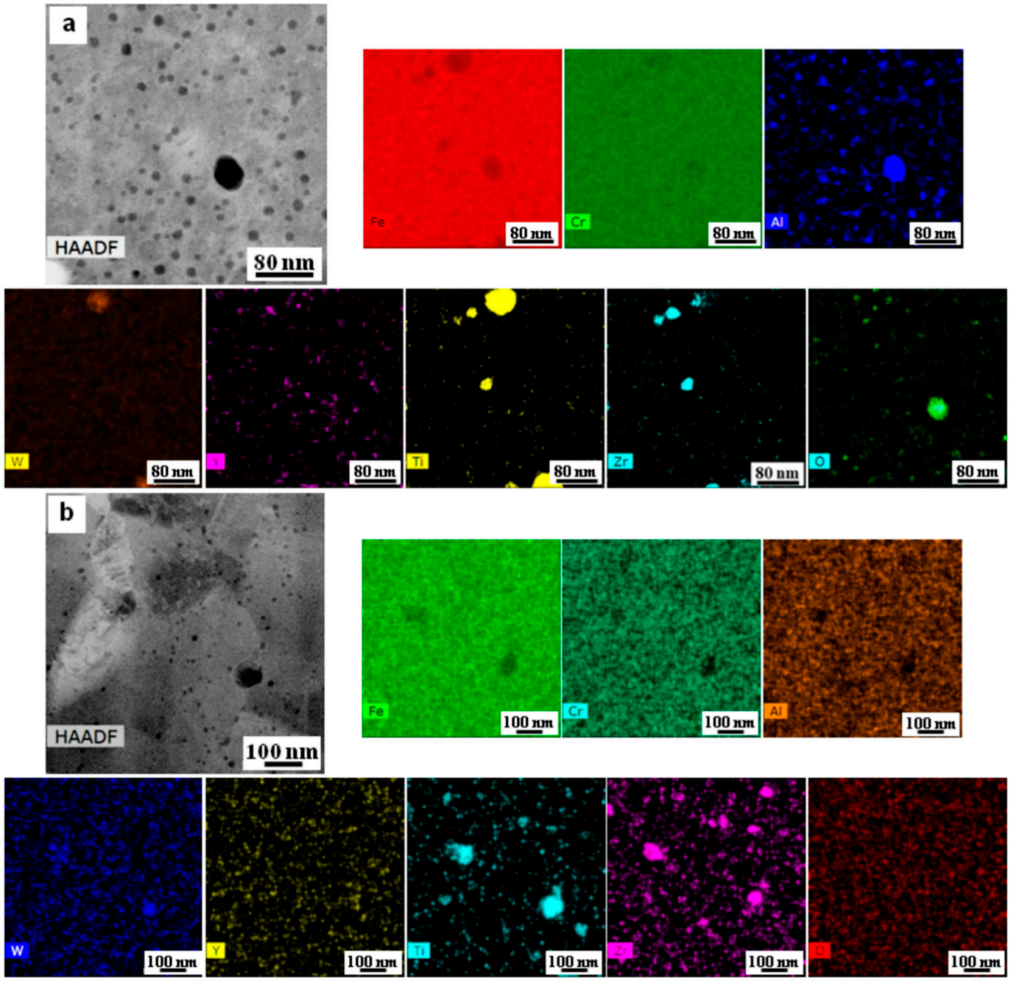

Figure 5. High angle annular dark field scanning transmission electron microscopy (HAADF-STEM) image and STEM-EDX elemental colour maps showing the oxides compositions in (**a**) ODS-0.45Zr, (**b**) ODS-0.60Zr.

The predominant compositions of these oxides are Y, Al, Ti, Zr, AlZr, AlTi, TiZr, YZr, YAl, YAlZr, YTiZr, YAlTi and YAlTiZr. The main difference found between the ODS samples, is that the percentage of oxides with Zr is significantly higher in the ODS-0.60Zr (67%) than in the ODS-0.45Zr (49%). On the other hand, the ODS-0.45Zr exhibits a higher percentage of oxides with Al (78%) than the ODS-0.60Zr (51%). In view of these results, it should be noted that the Zr addition is not avoiding the formation of Y-Al oxides, as it has been reported in the literature [12,32]. From the analysis of the oxide compositions, it is possible to conclude that small variations in the Zr content lead to significant differences in the concentration of the main precipitates formed within the ferritic matrix of these ODS alloys.

3.3. Mechanical Characterisation of SPS ODS Alloys

Vickers' microhardness measurements performed in the ODS specimens of this investigation (Figure 6) reveal that the addition of Zr increases noticeably the hardness in comparison with the same steel without Zr but with the same content of Al, Ti and Y_2O_3. This improvement is clearly due to the precipitation of Zr nano-oxides with different compositions, which are able to generate an Orowan strengthening by pinning effectively the movement of the dislocations created during the plastic deformation of the steel. The values reached are promising since they are higher than those reported in the literature for the hipped U14YW (14 wt.% Cr) and the hot extruded PM2000 (20 wt.% Cr) ODS steels, and in the range of the hot extruded MA957 (14 wt.% Cr) and 14GET (14 wt.% Cr) ODS alloys [33–36].

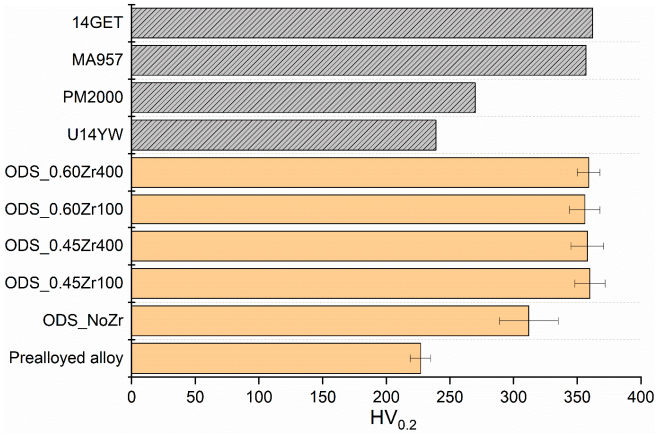

Figure 6. Microhardness of the ODS steels developed in this investigation and some ODS steels from the literature [33–36].

In addition, SP tests are performed on the ODS steels sintered by SPS in order to analyse more deeply the influence of the Zr nano-oxides on the mechanical behaviour of these materials. The load vs. deflection curves obtained for the different Zr contents (0.45 and 0.60 wt.%) and the selected heating rates (100 and 400 °C·min^{-1}) are shown in Figure 7. The mechanical behaviour is analysed at R.T., 300 and 500 °C in order to assess the stability and the adequacy of these new Zr dispersoids to retain the strength even at high temperatures. Furthermore, the maximum load values achieved in these SP tests at different temperatures are listed in Table 3. To compare the here-developed Zr ODS alloys with the ODS from GETMAT project, the data obtained for a similar SP test carried out on this alloy are also drawn in this graphic.

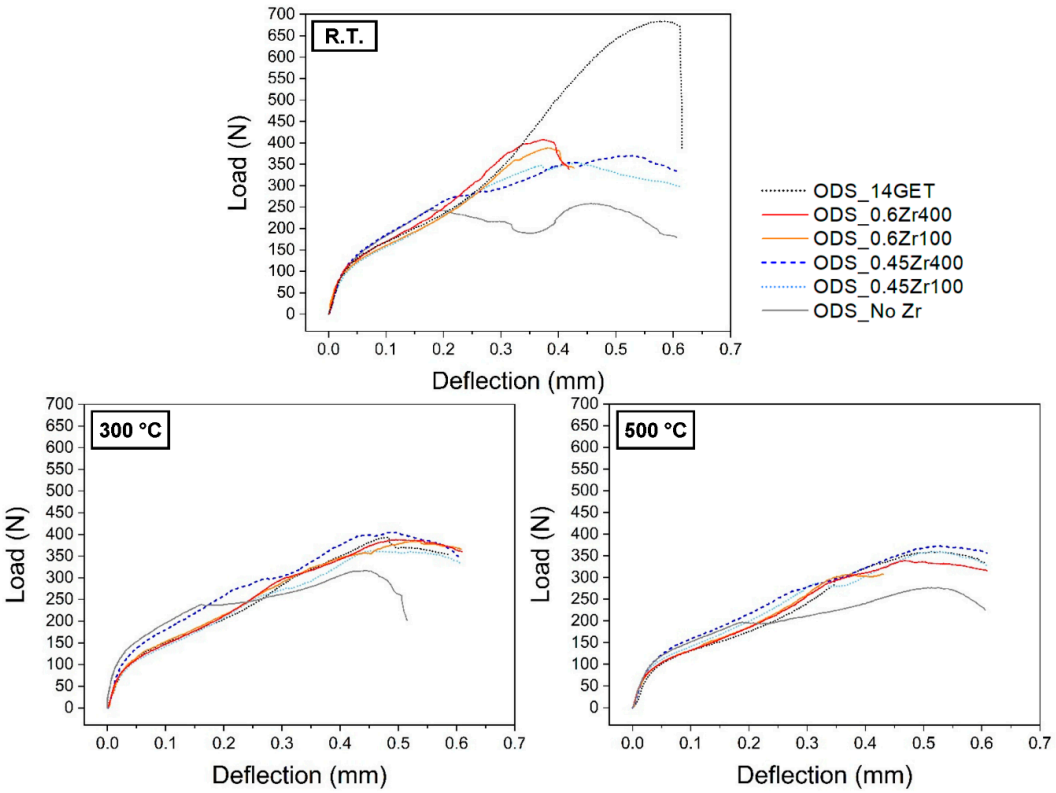

Figure 7. Load-deflection curves from small punch (SP) tests obtained at R.T., 300 and 500 °C for ODS sintered with different Zr contents and heating rates.

Table 3. Maximum load values reached at different temperatures during SP tests.

Sample ID	F_{max} (N) at R.T.	F_{max} (N) at 300 °C	F_{max} (N) at 500 °C
ODS_14GET	684	393	359
ODS_0.60Zr400	407	388	339
ODS_0.60Zr100	388	384	308
ODS_0.45Zr400	370	405	373
ODS_0.45Zr100	354	357	360
ODS_NoZr	258	317	251

The results indicate that the addition of Zr promotes indeed the precipitation of new highly stabilised nano-oxides serving as effective pinning points for the dislocation movement, and favouring the increase of the strength of the material at all the temperatures tested, in comparison to the ODS without Zr addition. In addition, these Zr nano-oxides contribute to a microstructure in which there exists more volume of ultrafine grains (Figure 2). Likewise, the increase of the heating rate during sintering has also promoted these ultrafine grain regions. Then, the Zr content and the heating rate are parameters affecting the volume occupied by ultrafine grains. These regions with fine grain size exhibit a higher quantity of grain boundaries also acting as barriers for the movement of the dislocations and hardening the material by a Hall-Petch effect [37,38]. As a result, a higher volume of equiaxed ultrafine grains within the matrix, linked to existence of a larger number of fine and stable dispersoids in the matrix, are parameters acting together to achieve the significant strength increase observed in the Zr-ODS samples when compared to the No Zr-ODS. Nevertheless, at room temperature the experimental curves also highlight that the maximum loads withstood by the new Zr ODS alloys are noticeably lower (354–407 N) than the maximum load achieved by the 14GET ODS (684 N). This 14GET ODS was processed following hot extrusion at 1100 °C and a subsequent annealing, which led to a microstructure formed by elongated ferritic grains with bimodal grain distribution and a strong <110> fibre texture along the extrusion direction [33]. The SPSed Zr ODS steels are also composed of a bimodal grain distribution (Figure 2). However, in these samples, the grains grow during the SPS process in many different orientations, which are related to the preferential paths followed by the electrical current going through the matrix. This results in the existence of many elongated micrometric grains that grow along different directions within the matrix, together with the existence of regions formed by more equiaxed ultrafine grains. In addition, no texture is found in the samples at the end of the SPS process. These differences in the grain shape and in the preferential grain orientation may be the responsible for achieving a lower strength in SPSed alloys than in the HEed steel tested at room temperature. Thus, these results suggest that, at room temperature, the grain boundary sliding is more favoured when the SP test is performed on a SPSed ODS microstructure than along the longitudinal section of a HEed ODS sample. On the other hand, the SP curves shown in Figure 7 do not indicate significant differences in the ductility exhibited by the SPed and HEed ODS samples tested in this investigation at room temperature.

At higher temperatures, the HEed 14GET ODS is considerably decreasing its strength, and the maximum load drops to 393 N at 300 °C, and 359 N at 500 °C. On the other hand, it is worthy remarking that the SPSed microstructure seems to be able to retain the levels of strength with the increase of the temperature up to 300 °C. If the temperature is further increased up to 500 °C, then the maximum load decreases slightly to the range 308–373 N in the SPSed samples with Zr. The trend of diminishing the strength with increasing temperature is expected since some dislocations will be able to overcome the pinning caused by the nano-oxides, and therefore their motion is activated by thermal mechanisms [39]. Furthermore, the increase of the temperature produces slight coarsening of the grain structure and the dispersoids size, which are thermally activated processes, also contributing to the decrease of the strength. With the increase of the temperature above 300 °C, not significant differences are found in the strength and ductility obtained for the different Zr contents or heating rates. At these temperatures,

the motion of dislocation is so promoted that small variations in the volume fraction of nano-oxides and grain boundaries seem to have a negligible effect on the mechanical properties.

The examination of the samples after the SP tests reveals a fracture with circumferential cracks, typical for small punch ductile behaviour, together with some secondary radial cracks, which also indicate the existence of some brittle behaviour (Figure 8). The cracks in radial direction correspond to an intergranular failure mode, as a consequence of their propagation through the grain boundaries by growth and coalescence of microcavities, as reported by Oñorbe et al. in their investigation of a 9Cr ODS tested at temperatures above 300 °C [40]. These results point toward a slight effect of the Zr content on the fracture appearance of the material. The non Zr-ODS shows a clear mix ductile-brittle behaviour, while increasing the Zr content decreases substantially the appearance of brittle radial cracks. The differences on the fracture samples also seem to indicate a slightly higher ductility for the 0.60Zr alloy, which is the SPSed sample with the highest Zr content.

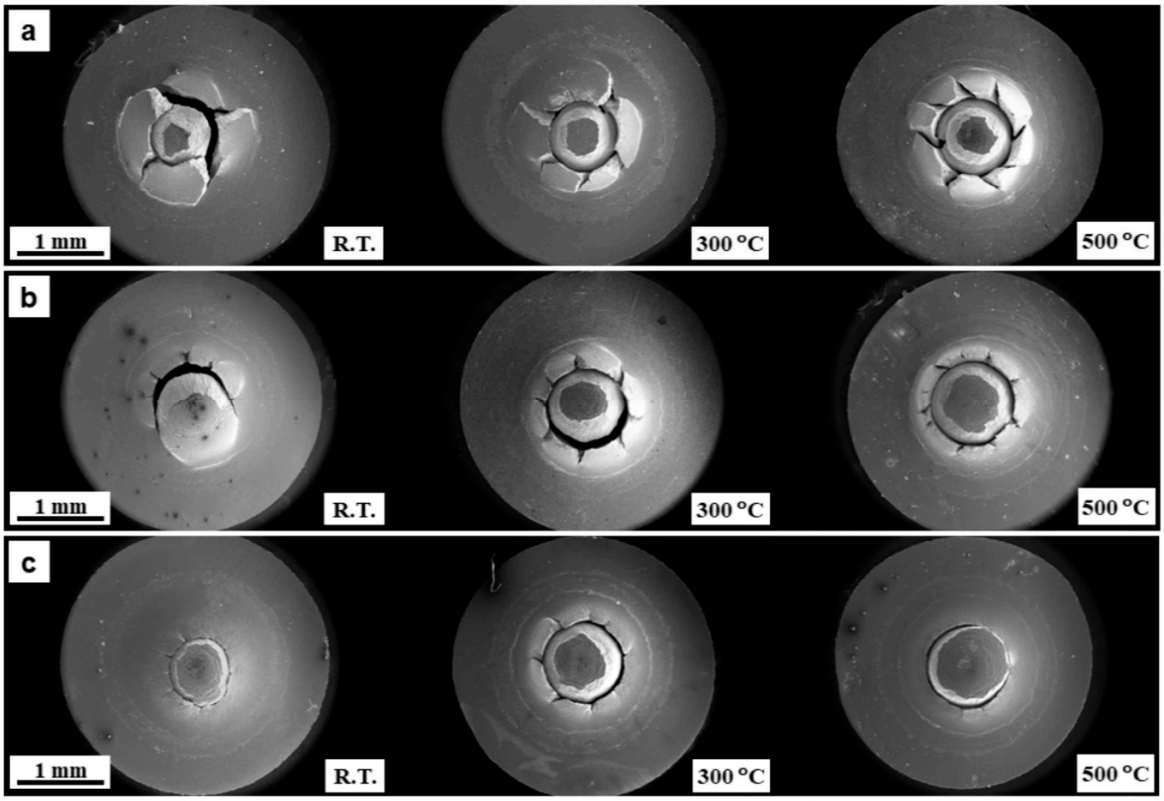

Figure 8. SEM images of small punch specimens after the fracture at R.T., 300 and 500 °C: (**a**) ODS-NoZr, (**b**) ODS-0.45Zr, (**c**) ODS-0.60Zr.

4. Conclusions

The effect of adding different Zr contents to a SPSed ODS steel on the microstructure and mechanical properties has been investigated in this study. The main conclusions are summarised as follows:

1. Zr can be effectively added as an elemental or oxide powder during the high-energy milling process. In both cases, Zr nano-oxides are formed after SPS consolidation of the ODS steel with an equivalent oxide number density. The oxide number density increases in an order of magnitude with respect to the ODS without Zr.
2. The Zr content has a clear effect on the final bimodal microstructure. A higher Zr quantity leads to the refinement of the microstructure and to the presence of larger regions formed by ultrafine ferritic grains. Zr nano-oxides are not homogeneously dispersed in the matrix, promoting smaller

grains in the regions with higher content of oxides. Thus, Zr nano-oxides are effective inhibitors of the grain growth during recrystallisation.

3. The increase of the heating rate during SPS involves shorter sintering times and leads to a microstructure with higher volumes of ultrafine grains, since the grain growth is a process thermally activated depending on time. The heterogeneous distribution of plastic deformation and alloying elements among powder particles, together with the different particle size distribution, lead to an abnormal grain size evolution during SPS consolidation.
4. Different combinations among Y, Al, Ti and Zr with oxygen are found in these ODS alloys. The final percentage of Zr nano-oxides is enlarged with the increase of the Zr content in the MA powders.
5. The average oxide size is refined by adding Zr from 12 nm diameter reached in the ODS without Zr to near 6 nm in the ODS with 0.6 wt.% of Zr.
6. Minor addition of Zr improves the mechanical behaviour of ferritic Al-containing ODS alloys at all the temperatures tested. The analysis of the SP curves obtained during the tests, suggests that the Zr nano-oxides dispersed within the matrix are acting as effective obstacles in pinning the dislocations and impeding their motion. In addition, these Zr dispersoids also act as barriers for the grain boundary movement. These phenomena, together with the existence of large regions of ultrafine grains increasing the strength by a Hall-Petch effect, are contributing to withstand considerable high loads during the SP tests.

Author Contributions: Conceptualisation, A.G.-J., M.C. and J.M.T.; methodology, A.G.-J., E.M., D.G. and M.S.; software, A.G.-J. and E.M.; validation, A.G.-J.; formal analysis, A.G.-J. and E.M.; investigation, A.G.-J. and E.M.; resources, A.G.-J., D.G., M.S. and M.C.; data curation, A.G.-J. and E.M.; writing—original draft preparation, A.G.-J.; writing—review and editing, A.G.-J.; visualisation, A.G.-J.; supervision, A.G.-J., J.M.T. and M.C.; project administration, M.C.; funding acquisition, M.C. All authors have read and agreed to the published version of the manuscript.

Funding: This research was funded by Ministerio de Economía y Competitividad, Gobierno de España (grant numbers MAT2013-47460-C5-5-P and MAT2016-80875-C3-3-R).

Acknowledgments: The authors would like to express their gratitude to Daniel Plaza for his kind help during the small punch tests.

Conflicts of Interest: The authors declare no conflict of interest.

References

1. Gong, M.; Zhou, Z.; Hu, H.; Zhang, G.; Li, S.; Wang, M. Effects of aluminum on microstructure and mechanical behavior of 14Cr–ODS steels. *J. Nucl. Mater.* **2015**, *462*, 502–507. [CrossRef]
2. Steckmeyer, A.; Praud, M.; Fournier, B.; Malaplate, J.; Garnier, J.; Béchade, J.L.; Tournié, I.; Tancray, A.; Bougault, A.; Bonnaillie, P. Tensile properties and deformation mechanisms of a 14Cr ODS ferritic steel. *J. Nucl. Mater.* **2010**, *405*, 95–100. [CrossRef]
3. Dou, P.; Sang, W.; Kimura, A. Morphology, crystal and metal/oxide interface structures of nanoparticles in Fe–15Cr–2W–0.5Ti–7Al–0.4Zr–0.5Y2O3 ODS steel. *J. Nucl. Mater.* **2019**, *523*, 231–247. [CrossRef]
4. He, P.; Hoffmann, J.; Möslang, A. Effect of milling time and annealing temperature on nanoparticles evolution for 13.5% Cr ODS ferritic steel powders by joint application of XAFS and TEM. *J. Nucl. Mater.* **2018**, *501*, 381–387. [CrossRef]
5. Hilger, I.; Tegel, M.; Gorley, M.J.; Grant, P.S.; Weißgärber, T.; Kieback, B. The structural changes of Y2O3 in ferritic ODS alloys during milling. *J. Nucl. Mater.* **2014**, *447*, 242–247. [CrossRef]
6. Ratti, M.; Leuvrey, D.; Mathon, M.H.; De Carlan, Y. Influence of titanium on nano-cluster (Y, Ti, O) stability in ODS ferritic materials. *J. Nucl. Mater.* **2009**, *386–388*, 540–543. [CrossRef]
7. Fournier, B.; Dalle, F.; Sauzay, M.; Longour, J.; Salvi, M.; Caës, C.; Tournié, I.; Giroux, P.-F.; Kim, S.-H. Comparison of various 9–12% Cr steels under fatigue and creep-fatigue loadings at high temperature. *Mater. Sci. Eng. A.* **2011**, *528*, 6934–6945. [CrossRef]

8. Kimura, A.; Kasada, R.; Iwata, N.; Kishimoto, H.; Zhang, C.H.; Isselin, J.; Dou, P.; Lee, J.H.; Muthukumar, N.; Okuda, T.; et al. Development of Al added high-Cr ODS steels for fuel cladding of next generation nuclear systems. *J. Nucl. Mater.* **2011**, *417*, 176–179. [CrossRef]
9. Takaya, S.; Furukawa, T.; Müller, G.; Heinzel, A.; Jianu, A.; Weisenburger, A.; Aoto, K.; Inoue, M.; Okuda, T.; Abe, F.; et al. Al-containing ODS steels with improved corrosion resistance to liquid lead–bismuth. *J. Nucl. Mater.* **2012**, *428*, 125–130. [CrossRef]
10. Kasada, R.; Toda, N.; Yutani, K.; Cho, H.S.; Kishimoto, H.; Kimura, A. Pre- and post-deformation microstructures of oxide dispersion strengthened ferritic steels. *J. Nucl. Mater.* **2007**, *367–370*, 222–228. [CrossRef]
11. Song, P.; Zhang, Z.; Yabuuchi, K.; Kimura, A. Helium bubble formation behavior in ODS ferritic steels with and without simultaneous addition of Al and Zr. *Fusion Eng. Des.* **2017**, *125*, 396–401. [CrossRef]
12. Gao, R.; Zhang, T.; Wang, X.P.; Fang, Q.F.; Liu, C.S. Effect of zirconium addition on the microstructure and mechanical properties of ODS ferritic steels containing aluminum. *J. Nucl. Mater.* **2014**, *444*, 462–468. [CrossRef]
13. Xu, H.; Li, W.; Sha, X.; Meng, J.; Kang, C.; Wang, W.; Zang, X.; Wang, Z. Effects of Zr addition on the microstructural stability of 15Cr-ODS steels under elevated-temperature annealing. *Fusion Eng. Des.* **2019**, *138*, 231–238.
14. Yabuuchi, A.; Maekawa, M.; Kawasuso, A. Influence of oversized elements (Hf, Zr, Ti and Nb) on the thermal stability of vacancies in type 316L stainless steels. *J. Nucl. Mater.* **2012**, *430*, 190–193. [CrossRef]
15. Isselin, J.; Kasada, R.; Kimura, A.; Okuda, T.; Inoue, M.; Ukai, S.; Ohnuki, S.; Fujisawa, T.; Abe, F. Effects of Zr addition on the microstructure of 14%Cr4%Al ODS ferritic steels. *Mater. Trans.* **2010**, *51*, 1011–1015. [CrossRef]
16. García-Junceda, A.; Campos, M.; García-Rodríguez, N.; Torralba, J.M. On the role of alloy composition and sintering parameters in the bimodal grain size distribution and mechanical properties of ODS ferritic steels. *Metall. Mater. Trans. A* **2016**, *47*, 5325–5333. [CrossRef]
17. Macía, E.; García-Junceda, A.; Serrano, M.; Díaz, L.A.; Campos, M. Effect of the heating rate on the microstructure of a ferritic ODS steel (Y-Ti-Al-Zr) consolidated by spark plasma sintering. *J. Nucl. Mater.* **2019**, *518*, 190–201. [CrossRef]
18. Hilger, I.; Boulnat, X.; Hoffmann, J.; Testani, C.; Bergner, F.; De Carlan, Y.; Ferraro, F.; Ulbricht, A. Fabrication and characterization of oxide dispersion strengthened (ODS) 14Cr steels consolidated by means of hot isostatic pressing, hot extrusion and spark plasma sintering. *J. Nucl. Mater.* **2016**, *472*, 206–214. [CrossRef]
19. Dapeng, Z.; Yong, L.; Feng, L.; Yuren, W.; Liujie, Z.; Yuhai, D. ODS ferritic steel engineered with bimodal grain size for high strength and ductility. *Mater. Lett.* **2011**, *65*, 1672–1674. [CrossRef]
20. Munir, Z.A.; Anselmi-Tamburini, U.; Ohyanagi, M. The effect of electric field and pressure on the synthesis and consolidation of materials: A review of the spark plasma sintering method. *J. Mater. Sci.* **2006**, *41*, 763–777. [CrossRef]
21. Auger, M.A.; De Castro, V.; Leguey, T.; Muñoz, A.; Pareja, R. Microstructure and mechanical behavior of ODS and non-ODS Fe–14Cr model alloys produced by spark plasma sintering. *J. Nucl. Mater.* **2013**, *436*, 68–75. [CrossRef]
22. FP7 Project Final Report: GEn IV and Transmutation MATerials, GETMAT 2013. Available online: https://cordis.europa.eu/project/id/212175/reporting (accessed on 5 March 2020).
23. Scherrer, P. Bestimmung der Grösse und der Inneren Struktur von Kolloidteilchen Mittels Röntgenstrahlen, Göttingen. *Math. Phys. Kl.* **1918**, *2*, 98–100.
24. García-Junceda, A.; Acebo, L.; Torralba, J.M. Study and suppression of the microstructural anisotropy generated during the consolidation of a carbonyl iron powder by field assisted hot pressing. *Metall. Mater. Trans. A* **2015**, *46*, 3192–3198. [CrossRef]
25. García-Junceda, A.; García-Rodríguez, N.; Campos, M.; Cartón-Cordero, M.; Torralba, J.M. Effect of Zr addition on the microstructure and mechanical properties of an Al-alloyed ODS steel consolidated by FAHP. *J. Am. Ceram. Soc.* **2015**, *98*, 3582–3587. [CrossRef]
26. CEN. Small Punch Test Method for Metallic Materials. In *CEN Workshop Agreement*; CWA 15627:2006(E); CEN: Brussels, Belgium, 2006.
27. Ressel, G.; Parz, P.; Primig, S.; Leitner, H.; Clemens, H.; Puff, W. New findings on the atomistic mechanisms active during mechanical milling of a Fe-Y_2O_3 model alloy. *J. Appl. Phys.* **2014**, *115*, 124313. [CrossRef]

28. Fuentes-Pacheco, L.; Campos, M.; Torralba, J.M. Thermal stability of nanostructured iron powder as a function of amount and nature of reinforcement (Nb or NbC). *Rev. Metal.* **2011**, *47*, 373–380. [CrossRef]
29. Molinari, A.; Libardi, S.; Leoni, M.; Scardi, P. Role of lattice strain on thermal stability of a nanocrystalline FeMo alloy. *Acta Mater.* **2010**, *58*, 963–966. [CrossRef]
30. Guillon, O.; Gonzalez-Julian, J.; Dargatz, B.; Kessel, T.; Schierning, G.; Räthel, J.; Herrmann, M. Field-Assisted Sintering Technology/Spark Plasma Sintering: Mechanisms, Materials, and Technology Developments. *Adv. Eng. Mater.* **2014**, *16*, 830–849. [CrossRef]
31. Dou, P.; Kimura, A.; Kasada, R.; Okuda, T.; Inoue, M.; Ukai, S.; Ohnuki, S.; Fujisawa, T.; Abe, F. TEM and HRTEM study of oxide particles in an Al-alloyed high-Cr oxide dispersion strengthened steel with Zr addition. *J. Nucl. Mater.* **2014**, *444*, 441–453. [CrossRef]
32. Takaya, S.; Furukawa, T.; Inoue, M.; Fujisawa, T.; Okuda, T.; Abe, F.; Ohnuki, S.; Kimura, A. Corrosion resistance of Al-alloying high Cr–ODS steels in stagnant lead–bismuth. *J. Nucl. Mater.* **2010**, *398*, 132–138. [CrossRef]
33. García-Junceda, A.; Hernández-Mayoral, M.; Serrano, M. Influence of the microstructure on the tensile and impact properties of a 14Cr ODS steel bar. *Mater. Sci. Eng. A* **2012**, *556*, 696–703. [CrossRef]
34. Oksiuta, Z.; Baluc, N. Effect of mechanical alloying atmosphere on the microstructure and Charpy impact properties of an ODS ferritic steel. *J. Nucl. Mater.* **2009**, *386–388*, 426–429. [CrossRef]
35. Alinger, M.J.; Odette, G.R.; Hoelzer, D.T. On the role of alloy composition and processing parameters in nanocluster formation and dispersion strengthening in nanostructured ferritic alloys. *Acta Mater.* **2009**, *57*, 392–406. [CrossRef]
36. Torralba, J.M.; Fuentes-Pacheco, L.; García-Rodríguez, N.; Campos, M. Development of high performance powder metallurgy steels by high-energy milling. *Adv. Powder Technol.* **2013**, *24*, 813–817. [CrossRef]
37. Hall, E.O. The deformation and ageing of mild steel: III Discussion of Results. *Proc. Phys. Soc. B* **1951**, *64*, 747–753. [CrossRef]
38. Petch, N.J. The cleavage strength of polycrystals. *J. Iron Steel Inst.* **1953**, *174*, 25–28.
39. Siska, F.; Stratil, L.; Hadraba, H.; Fintova, S.; Kubena, I.; Zalezak, T.; Bartkova, D. High temperature deformation mechanisms in the 14% Cr ODS alloy. *Mater. Sci. Eng. A* **2017**, *689*, 34–39. [CrossRef]
40. Oñorbe, E.; Hernández-Mayoral, M.; Morrison, A.; Serrano, M. Study of the microstructure and small punch behavior of a 9Cr ODS tube. *Nucl. Mater. Energy* **2019**, *20*, 100698. [CrossRef]